Scalable creation of spin-photon interfaces for solid-state quantum information processing

by

Noel H. Wan

B.A., Columbia University (2014)

Submitted to the Department of Electrical Engineering and Computer Science
in partial fulfillment of the requirements for the degree of

Master of Science in Electrical Engineering and Computer Science

at the

MASSACHUSETTS INSTITUTE OF TECHNOLOGY

February 2017

Author ..... Signature redacted
Department of Electrical Engineering and Computer Science
January 20, 2017

Certified by .. Signature redacted .....
Dirk R. Englund
Associate Professor of Electrical Engineering and Computer Science
Thesis Supervisor

Accepted by ... Signature redacted .....
Leslie A. Kolodziejski
Chair, Department Committee on Graduate Theses

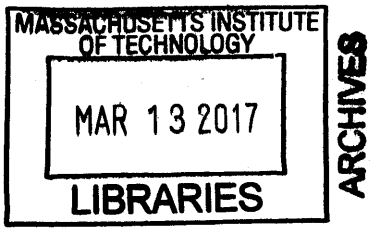

Scalable creation of spin-photon interfaces for solid-state quantum information processing

by

Noel H. Wan

Submitted to the Department of Electrical Engineering and Computer Science
on January 20, 2017, in partial fulfillment of the
requirements for the degree of
Master of Science in Electrical Engineering and Computer Science

Abstract

The negatively charged nitrogen vacancy (NV) defect center in diamond is a promising solid-state qubit due to its exceptional spin and optical properties. In this thesis, we develop high-yield, efficient spin-photon interfaces in diamond. In particular, we demonstrate a process that produces dielectic reflectors and photonic crystal nanobeam cavities directly on the surface of bulk diamond. Our results pave the way towards a scalable network of entangled quantum registers based on spin qubits in diamond.

Thesis Supervisor: Dirk R. Englund
Title: Associate Professor of Electrical Engineering and Computer Science

Acknowledgments

First and foremost, I would like to express my sincere appreciation to Professor Dirk Englund. His enthusiasm and knowledge in a wide range of topics is inspiring. Most importantly, Professor Englund creates a stimulating work environment by always being available to discuss new ideas and provide constructive feedback - often with creative solutions. With his guidance, I look forward to further develop my interests and skills as a scientist over the coming years.

Next, I would like to thank Professor Tim Schröder who supervised many projects during his postdoctoral fellowship at MIT. Professor Schröder provided guidance to many younger students in the lab but also proactively contributed to many projects from the development stage to the final result. His presence will be missed.

Most of the work on nanocavity diamond nanofabrication was done in close collaboration with Sara Mouradian, without whom this work is not possible. Almost the entirety of our improved diamond nanofabrication can be credited to her optimism in the face of missing diamonds and disastrous etches. I would also like to thank Michael Walsh, Hyeongrak Choi and Eric Bersin for their work on the characterization setup (Chapter 5), a critical process for the creation of high-yield cavity-coupled NV centers.

Donggyu Kim and Benjamin Lienhard also selflessly dedicated their time with the diamond reflector measurements and I am very thankful for their help. I am also grateful to the new PhDs Dr Edward Chen, for teaching me my first quantum optics, and Dr Luozhou Li, for guiding me through the basics of nanofabrication. I would also like to acknowledge Tsung-Ju Lu for trading cleanroom techniques and Jim Daley, Mark Mondol and Tim Savas of the NanoStructures Laboratory for helping me develop my etch and lithography recipes.

Everyone above and many others have been instrumental to the outcome of this thesis but above all, my partner and family have singly contributed the most. Their constant support is always a source of motivation and I cannot thank them enough for their love.

Contents

List of Figures

Chapter 1

Parabolic reflectors in bulk diamond for enhanced collection efficiency

Diamond is a host to many promising solid-state qubits such as the nitrogen-vacancy (NV) center, silicon-vacancy center, germanium-vacancy center, and many more. For applications in quantum information processing as well as in quantum-enhanced metrology, the emitted photon from the NV center must be efficiently collected[1, 2]. However, only photons emitted within a half-cone angle of $\sin^{-1}(1/n) = 24°$ can be collected due to the high refractive index when they are within bulk diamond ($n = 2.4$), limiting the maximum collection efficiency to ~5%.

Previous works have overcome total internal refraction (TIR) by fabricating solid-immersion lenses (SIL) on individual NV centers [3, 4]. This approach effectively increases the numerical aperture by n; therefore, only emission in the upper hemisphere can be extracted from the diamond. Further, the emission from such a structure is not highly directional, and SILs demonstrated so far were produced by focused ion beam (FIB) milling, which is a sequential and overall slow process.

In this chapter, a microfabricated structure that allows for broadband collection of ~ 70-80% of the emission from the NV zero-phonon line (ZPL) and phonon sideband is presented. The structure is presented in Figure 1-1(a). Total internal refraction is used to reflect photons emitted into solid angles of $\sim [\tan^{-1}(r/h), -\tan^{-1}(r/h)]$ where r and h are the radius and height of the structure, respectively. To improve

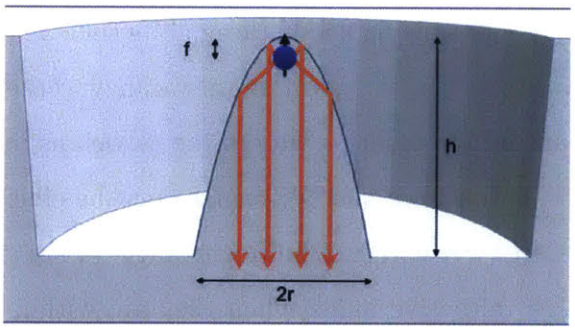

Figure 1-1: Emission from the NV center is redirected such that >60-80% can be efficiently collected from one direction

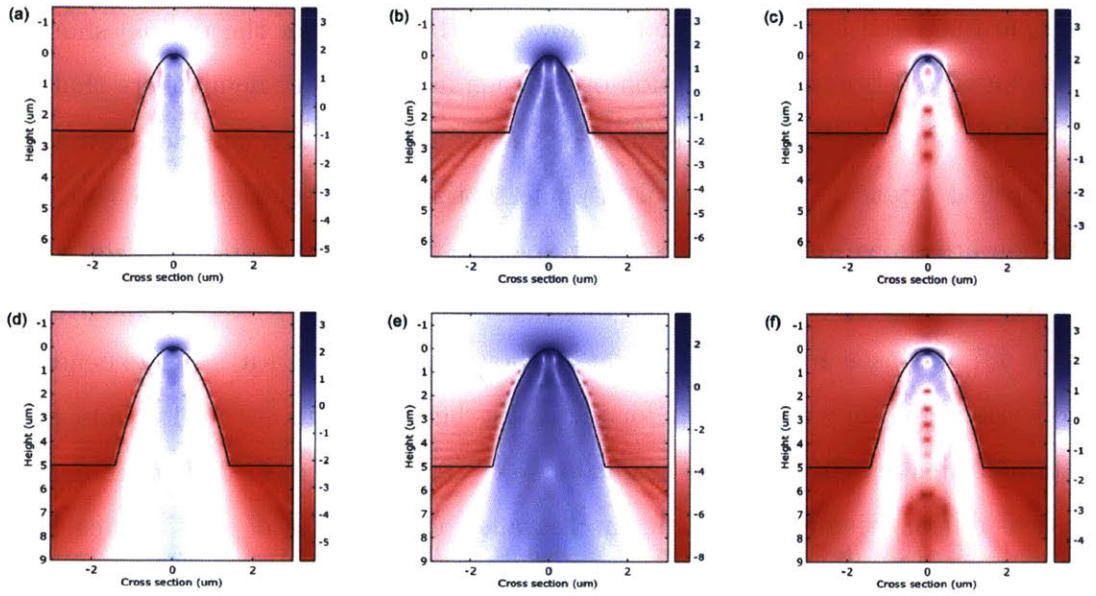

Figure 1-2: Emission pattern for dipole in a reflector with $(f, h) = (0.1, 2.5)$ μm: (a) horizontal, in-plane orientation (b) horizontal, out of-plane orientation (c) vertical orientation. Emission pattern for dipole in a reflector with $(f, h) = (0.1, 5)$ μm: (a) horizontal, in-plane orientation (b) horizontal, out of-plane orientation (c) vertical orientation

directionality, the structure should be paraboloidal with the emitter located at the focal point. In the next sections, the design of the structure is further discussed and a method to produce numerous such structures is presented. Experimental results are then described and future work is subsequently discussed.

1.1 Device principle

To maintain narrow linewidths and stable optical transitions at low temperatures, deep (<100 nm) NV centers are preferred [5]. Therefore, a focus of $f = 100$ nm equivalent to the NV implantation depth (from Stopping and Range of Ions in Matter (SRIM) simulations) is chosen. The equation of a parabola

$$z = \frac{x^2}{4f} \tag{1.1}$$

can be parametrized by its focus alone. However, the height (or the radius) should also be considered because the fraction of emission into the lower hemisphere that is redirected by the structure is determined by the aspect ratio. The emission patterns for an optical dipole with horizontal in-plane, horizontal out-of-plane and vertical orientation are shown in Figure 1-2(a-c), respectively, for $(f, h) = (0.1, 2.5)$ μm and for $(f, h) = (0.1, 5)$ μm in Figure 1-2(d-f), respectively. The collection efficiency for $\lambda = 637$ nm as a function of height is shown in Figure 1-3(a). As expected, the collection efficiency is constant for increasing height within NA = 1.3, and the collection efficiency increases with height for NA = 0.5. Solid (dashed) lines indicate an optical dipole oriented perpendicular (parallel) to the reflector axis. Since the reflector has a cylindrical symmetry, the collection efficiencies for an arbitrary dipole orientation must lie within the shaded areas, as verified by finite-difference time-domain simulations.

At $h = 5$ μm, the collection efficiency initially increases with focus and remains constant after $f = 50$ nm, as shown in Figure 1-3(b). This high collection efficiency is maintained across the NV ZPL and phonon sideband, as shown in Figure 1-4. The collection efficiency from a NV in a parabolic reflector is 15$\times$ greater than that from planar bulk diamond.

Although other photonic devices in bulk diamond can in principle achieve higher collection efficiencies, they are typically sensitive to emitter displacement and fabrication imperfections. As such, count rates of $\sim$1 Mega counts per second (Mcps) are typically reported. Such count rates are comparable to that obtained from NV in a SIL. The drop in performance is expected as these devices are based on waveguides, interference or cavity effects, all of which depend sensitively on the emitter's position. As in the case of the SIL, the enhancement of collection efficiency here is due to geometrical considerations and as such the structure would be robust to emitter displacement and fabrication imperfections.

The sensitivity to vertical and lateral displacements are shown in Figure 1-5(a-b). hen the emitter is 500 nm below the focal plane, the reflector maintains a collection efficiency within 75% (20%) of its maximum value and retains its maximum collection

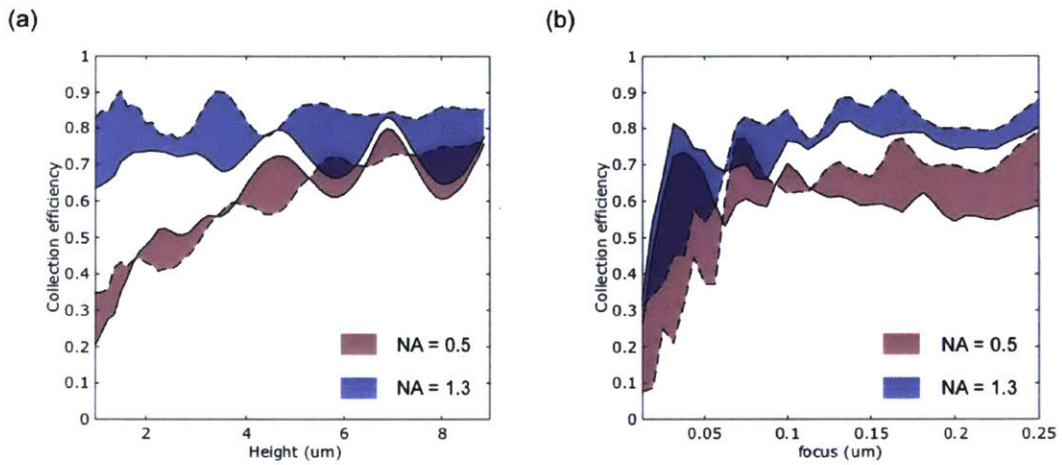

Figure 1-3: Solid (dashed) lines indicate a dipole oriented perpendicular (parallel) to the reflector axis. In (a), the height of the reflector is increased (focus = 100 nm). In (b) the focus is increased (height = 5 μm).

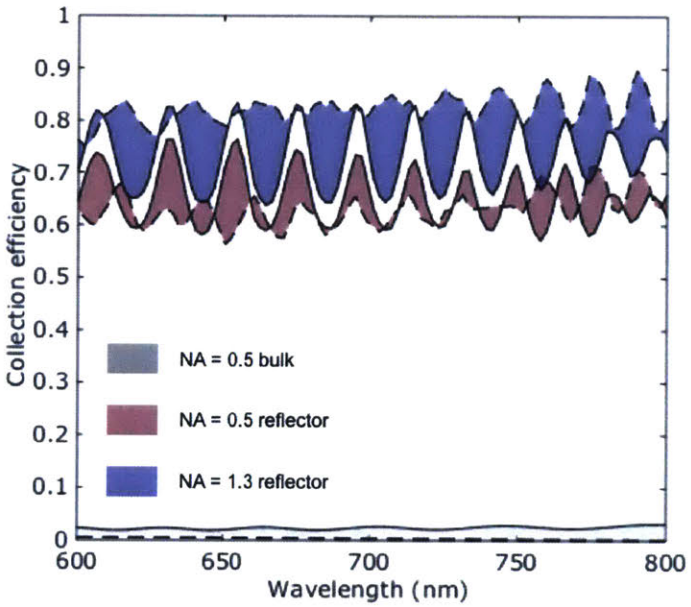

Figure 1-4: More than 60(70)% of the NV emission is redirected to within an NA of 0.5 (1.3), showing high efficiency and directionality. The collection efficiency is enhanced by 15X when the NV is placed in a reflector compared to an NV in planar bulk diamond. Solid (dashed) lines indicate a dipole oriented perpendicular (parallel) to the reflector axis. $f = 100$ nm and $h = 5\mu$m.

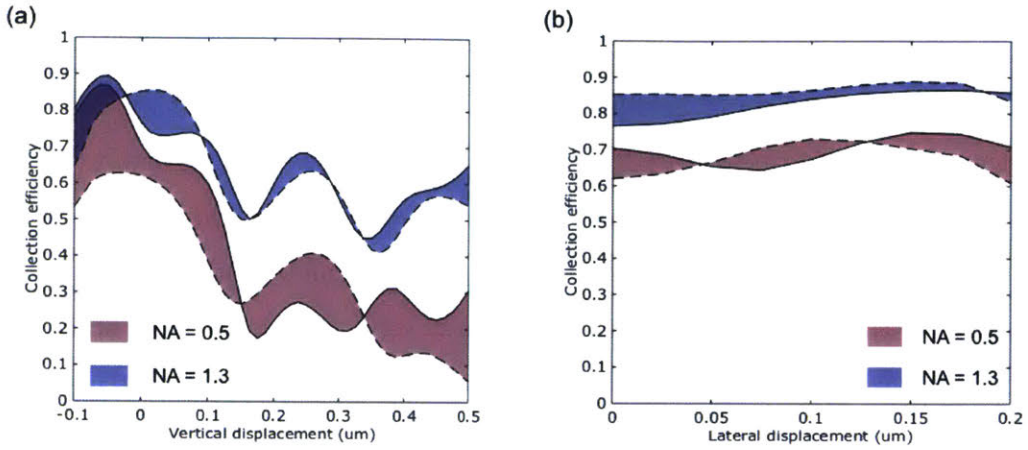

Figure 1-5: The reflector is robust to emitters that are (a) vertically and (b) laterally displaced from the focus. Solid (dashed) lines indicate a dipole oriented perpendicular (parallel) to the reflector axis. When the emitter is 500 nm below the focal plane, the reflector maintains a collection efficiency within 75% (20%) of its maximum value and retains its maximum collection efficiency for laterally displaced emitters. Therefore, the parabolic reflector is robust to both targeted fabrication and implanted NVs (where straggle is typically $\sim$40 nm^3).

efficiency for laterally displaced emitters. Therefore, the parabolic reflector is robust to both targeted fabrication and implanted NVs (where straggle is typically $\sim$40 nm^3). For vertically displaced emitters, the collection efficiency can be boosted by truncating the paraboloid such that upward emission that is within a half-cone of the critical angle is replaced with a surface that fulfills the TIR condition, as discussed further in the next section.

1.2 Fabrication of parabolic reflectors

Grayscale etching is required in order to incorporate standard oxygen plasma-based RIE processes, which are known to preserve the spin coherence of NV centers [6]). However, grayscale patterning is difficult to achieve with through electron beam lithography. Focused ion beam (FIB) milling is one relatively straightforward technique to carve 3D surfaces in diamond. However, it is a serial technique with low throughput. Further, heavy gallium ions are damaging and can be implanted in the diamond lattice in this process [3]. In this section, a novel approach based on standard top-down reactive-ion etching (RIE) is developed to fabricate parabolic structures. The fabrication process is shown in Figure 1-6.

First, NV centers are created in a 1 mm x 1 mm x 20 μm bulk diamond through a combination of nitrogen implantation and high temperature annealing, as detailed in Chapter 3. Then, global and local alignment marks are etched into the bulk diamond. NV centers are localized to within $\sim$30 nm and registered with a widefield characterization setup. This procedure is also described in Chapter 5. As shown in Figure 1-6(b), a silicon nitride (SiN) hard mask is then deposited on the diamond chip. Electron beam resist (EBR) is then spincoated on the hard mask, and electron beam lithography (EBL) defines an annulus in the EBR over the registered NV center. The EBR is then thermally reflowed above its glass transition temperature to assume a hemispherical profile. The pattern is then transferred into the SiN using fluorine-based RIE chemistry as shown in Figure 1-6(d). Due to the different etch rates in RIE, the etched SiN hardmask departs from being hemispherical to become paraboloidal. Here, both the SiN and EBR thickness are optimized parameters for a particular etch selectivity. Finally, the SiN pattern is transferred into bulk diamond using inductively coupled oxygen plasma reactive-ion etching (ICP-RIE). At this step, the etch is terminated before the center of the diamond paraboloid is subjected to etching to protect the single NV centers, resulting in a truncated parabolic reflector. In addition, as we will demonstrate, such structures also provide superior collection efficiency and signifcant tolerance to emitter straggle. The resulting reflectors (with-

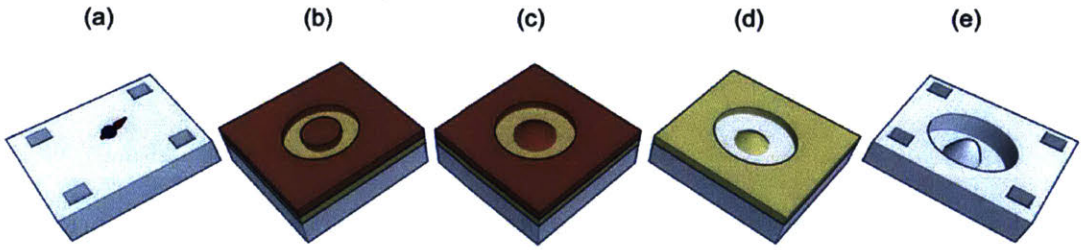

Figure 1-6: Process flow for producing parabolic reflectors in diamond. (a) First, global and local alignment marks are etched in diamond and NV centers are localized and registered (See Chapter 5). (b) Silicon nitride, which serves as our hard mask, is deposited and positive-tone electron beam resist is spincoated on the hard mask. An annulus is defined in the resist by electron beam lithography. (c) The resist is reflowed at its glass transition temperature. (d) The resist pattern is transferred into the hard mask by reactive-ion etching. (e) Paraboloids are etched into diamond by inductively coupled plasma reactive-ion etching.

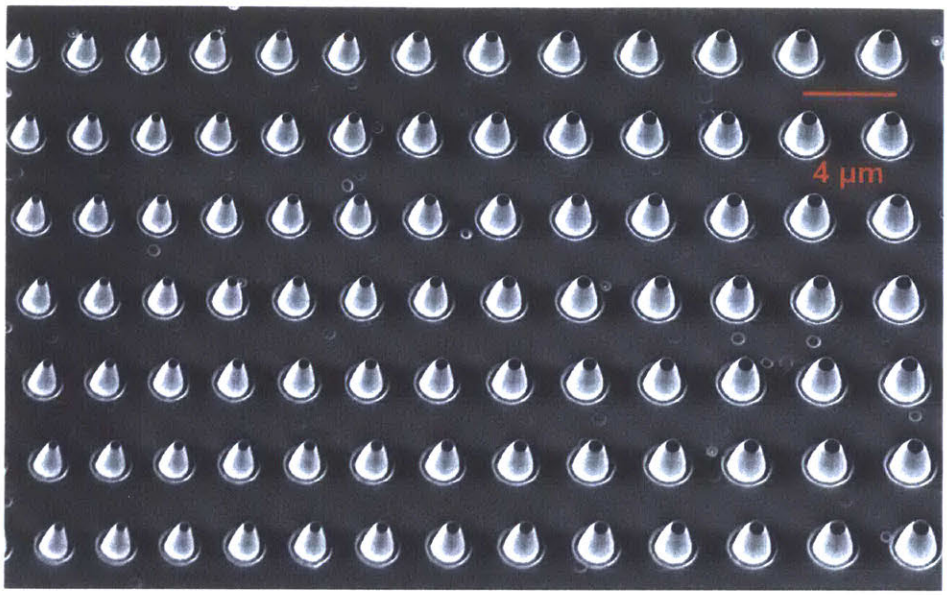

Figure 1-7: Scanning electron micrograph of an array of parabolic reflectors fabricated using the process in Figure 1-6.

out NV localization) are shown in Figure 1-7. Deterministic placement of parabolic reflectors on registered NV centers is shown in Figure 1-8.

Reflectors that contain a single NV center are studied in a confocal photoluminescence microscope and their surface qualities are characterized using atomic force microscopy (AFM). The AFM cross-section of a truncated Reflector A is shown in black in Figure 1-9(a) along with the location of its single NV. As shown, the cross-section is parabolic (red) with a focal plane of $\Delta z = 480$ nm from the NV. As discussed, truncated paraboloids can further boost the collection efficiency by redirecting incident photons that make an angle of $\theta < \theta_{cric}$ with the paraboloid. The collection efficiency of a truncated paraboloid is examined in Figures 1-9(b-d). For a perfectly located emitter i.e. $\Delta z = 0$ nm, the paraboloid surface from h - 30 nm do

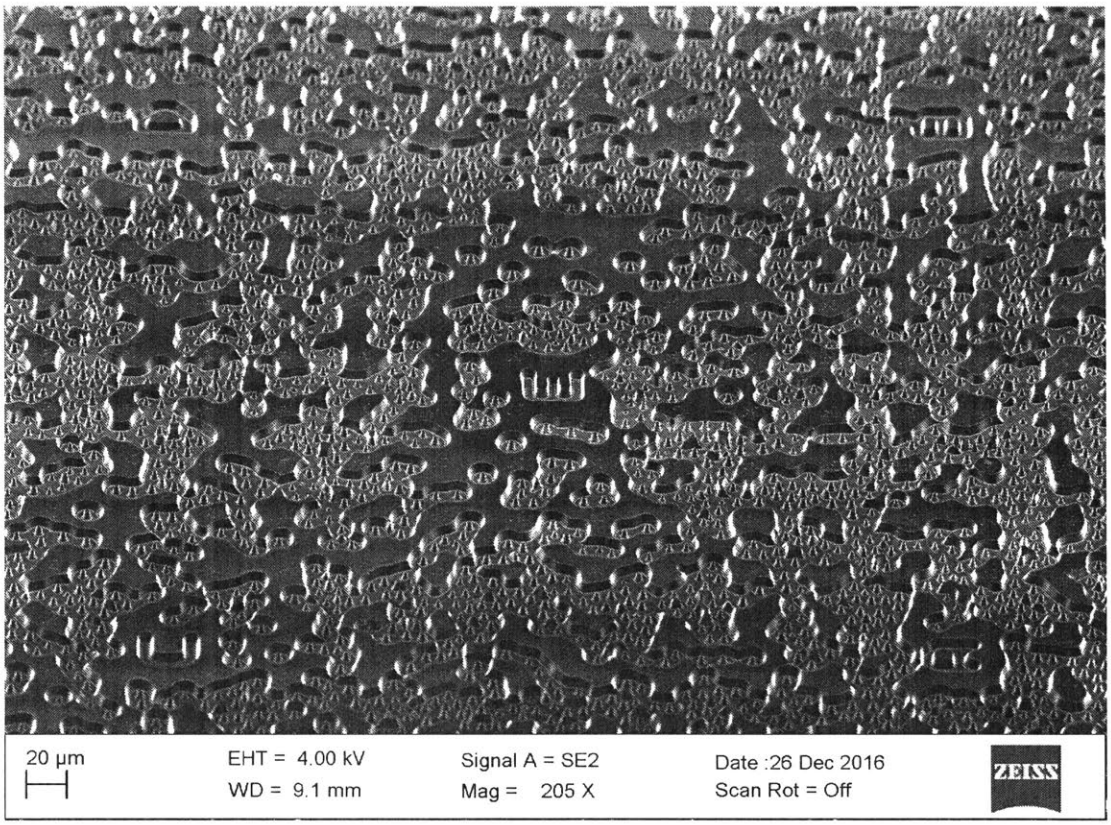

Figure 1-8: Scanning electron micrograph demonstrating deterministic placement of reflectors on registered NV centers.

not contribute to TIR; truncating at this plane would boost the efficiency by 2-3% (curves in Figure 1-9(d) gray and blue). This gain is small and requires more stringent fabrication precision. However, the truncation is particularly useful for vertically displaced emitters such as the NV in Reflector A. In particular, the ideal plane to truncate Reflector A is indicated by the gray dashed line in Figure 1-9(c) and the actual truncated plane is indicated by the blue solid line. As shown in Figure 1-9(d), when the NV resides at Δz =480 nm and the paraboloid is truncated, the collection efficiency increases from ~60% (gray curve) to ~87% (red curve).

1.3 Photon flux exceeding 1 Mcps

The parabolic reflectors is characterized in a homebuilt confocal fluorescence microscope (100X oil immersion objective, NA = 1.3). The diamond is placed on a "No.1" cover slip and imaged from the bottom as shown in Figure 1-10(b). NV centers are excited with a 532 nm diode laser and their photoluminescence spectra are recorded. NV centers are confirmed by their distinct spectra and optically detected magnetic resonance. About 1 in 10 of the fabricated structures contains single NV centers, as verified by second-order correlation measurements. (Annealing the diamond could increase the NV yield.).

After single NV centers have been confirmed, their count rates as a function of incident power are recorded. The count rate is fitted to a two-level emitter saturation model

$$I(P) = \frac{I_{sat}}{P_{sat} + P} P + cP + \text{dark counts} \tag{1.2}$$

where P is the power at the sample plane, cP is the linear background contribution, P_{sat} is the saturation power and I_{sat} is the count rate at saturation.

The background-corrected saturation curve for an NV in the bulk area (gray) and NV in Reflector A are plotted in Figure 1-11. For an NV located in bulk diamond, the typical I_{sat} is ~0.2 Mega counts per seconds (Mcps) and a P_{sat} of $88\mu W$. The NV in Reflector A has a count rate of I_{sat} = 2.93 Mcps, which represents over 12X enhancement of count rates from a single NV center. For the NV in reflector, the

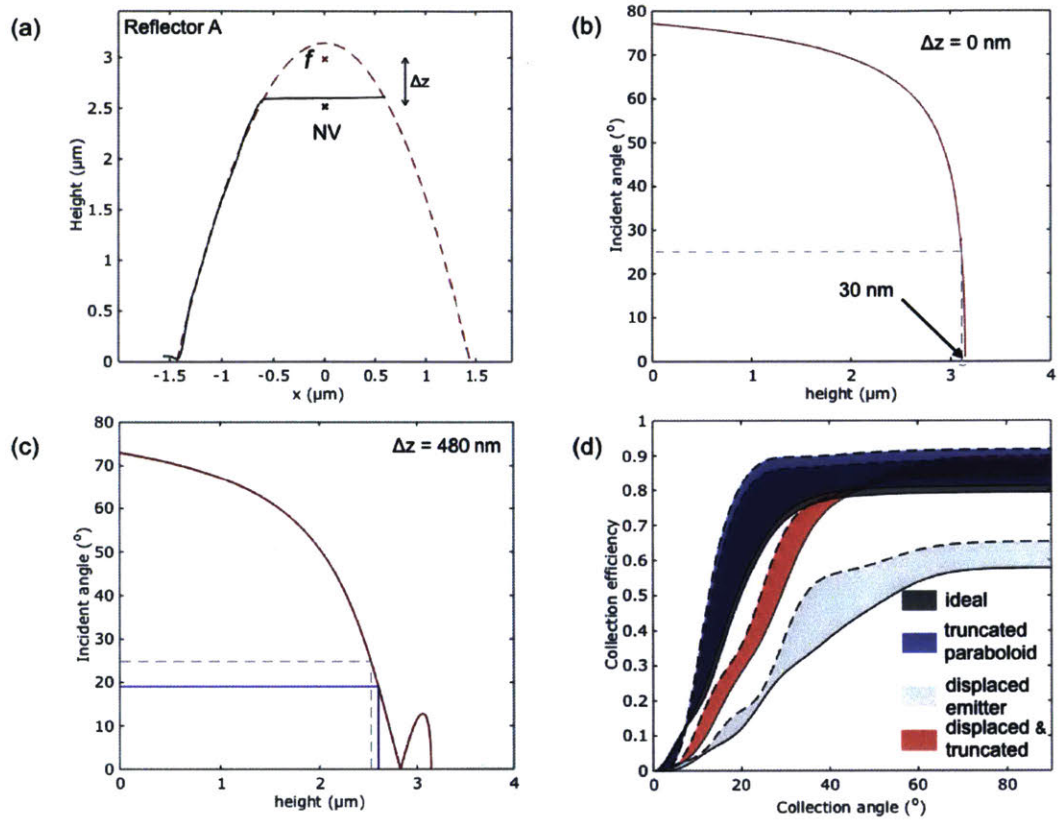

Figure 1-9: Boosting the collection efficiency from displaced emitters by truncating the paraboloid. (a) Atomic force microscope (AFM) line scan (black) and quadratic fit (red) of a truncated parabolic reflector A, yielding $f = 160$ nm. The red cross is the focus of the parabolic reflector and the black cross is the location of the NV center, 480 nm displaced from the focal plane. As discussed earlier, the reflector is robust to vertical straggle and figure (d) confirms that the collection efficiency of such a structure (gray curve) is within 75% of the maximum collection efficiency (black curve). The collection efficiency can be boosted by truncating the parabola at a height at which the photon's incident angle is less than the critical angle for total internal refraction (TIR). Figures (b) and (c) show the incident angle vs. the y-coordinate of the structure for a reflector with displacement $\Delta z = 0$ and $\Delta z = 480$ nm, respectively, and the location of ideal truncation. Figure (d) shows the collection efficiency of a structure with $\Delta z = 480$ nm can be boosted to >85%, comparable to the ideal setting. Solid (dashed) lines indicate a dipole oriented perpendicular (parallel) to the reflector axis.

Figure 1-10: Emission from the NV is collected from the bottom in a confocal setup. Microwave striplines can be used for spin driving.

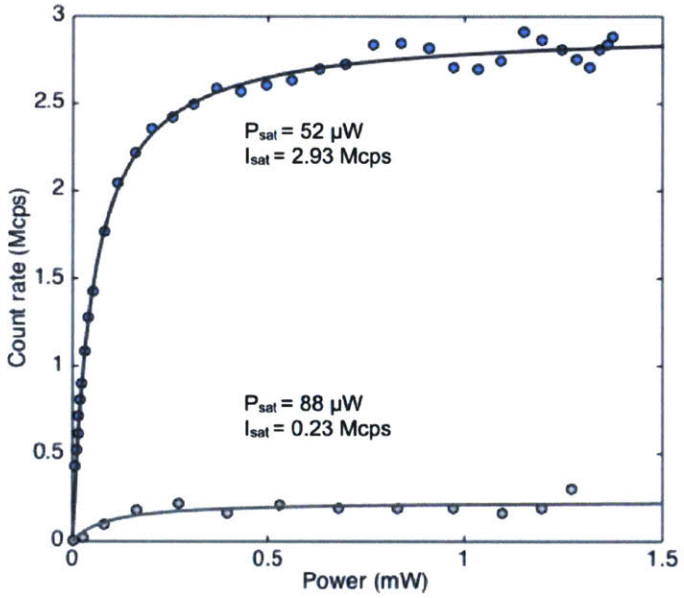

Figure 1-11: Background-corrected saturation curves for NV in bulk diamond (gray) and NV in parabolic reflector A (blue). The saturation curve is fitted to $I(P) = \frac{I_{sat}}{P_{sat}+P}P + cP +$ dark counts where cP is the linear background contribution. Reflector A enhances the collection efficiency from a single NV center by more than a factor of 10, yielding a saturation power P_{sat} count rate of $I_{sat} = 2.93$ Mcps.

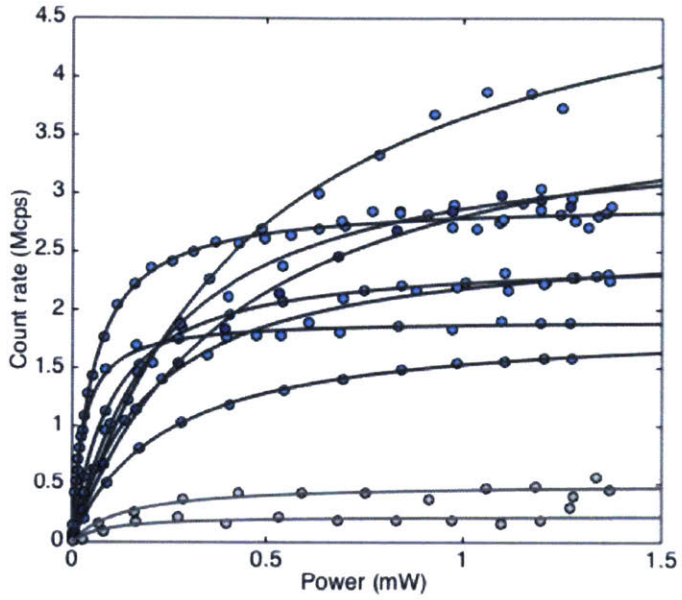

Figure 1-12: Background-corrected saturation curves for various NV in bulk diamond (gray) and NV in parabolic reflectors (blue).

lower saturation power also suggests an enhancement in excitation efficiency, which can be attributed to the focusing effect due to the structure. This measurement is repeated for other reflectors containing single NV centers. Their saturation curves are shown in Figure 1-12.

To quantify the quality of the single photon emission, a second-order intensity correlation measurement

$$g^{(2)}(\tau) = \frac{\langle I(t)(I(t+\tau)\rangle}{\langle I(t)\rangle^2} \tag{1.3}$$

is performed using a Hanbury-Brownn and Twiss configuration. The autocorrelation measurements at various excitation powers are shown in Figure 1-13. At half the saturation power, $g^{(2)}(0) = 0.06$ is obtained, therefore confirming low background from the reflector. The excitation power is gradually increased and pronounced anti-

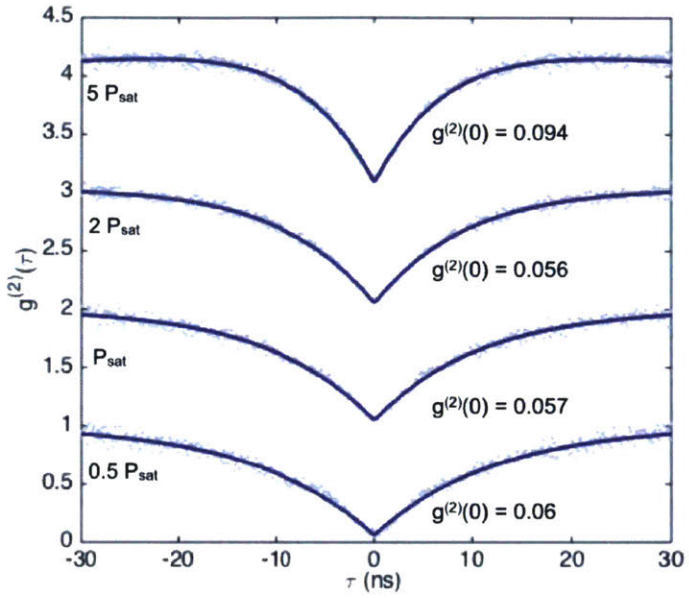

Figure 1-13: Second-order correlation measurement showing pronounced photon anti-bunching ($g^{(2)} < 0.1$) at various excitation powers.

bunching is observed up to $5P_{sat}$.

Excellent $g^{(2)}(0)$ values are also maintained when the pinhole (spatial filtering) is removed from the setup. The measured values of $g^{(2)}(0) < 0.25$ up to $5P_{sat}$ indicate a high single photon signal-to-noise ratio. Remarkably, $g^{(2)}(0) = 0.431$ is obtained even at $10P_{sat}$, as demonstrated in Figure 1-14. The increased $g^{(2)}(0)$ values can be attributed to fluorescence from emitters within the 20 μm-thick bulk diamond and background fluorescence from the immersion oil.

1.4 Outlook and current work

The measured parabolic reflectors yield count rates of up to 3 Mcps, which represents a 3$\times$ enhancement over the photon flux measured from microfabricated diamond solid

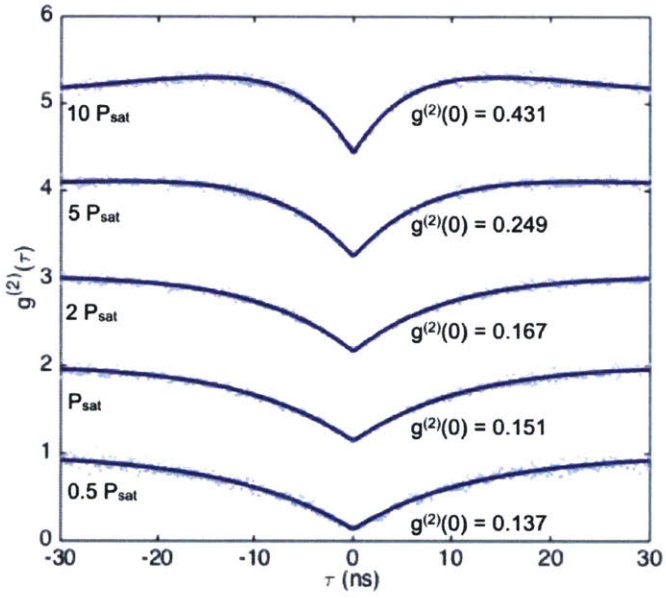

Figure 1-14: Pinhole (spatial filtering) is removed from the confocal setup and photon anti-bunching is maintained up to 10 P_{sat}, demonstrating the low background nature of the reflector and the fabrication process.

immersion lenses [3, 7]. To improve the current NV-NV entanglement scheme [8] rate which is tolerant to photon loss, the collection efficiency needs to be improved, which would be revealed by pulsed excitation measurements.As on-chip microwave delivery (see Figure 1-1) and dc control are straightforward to implement on the surface of the bulk diamond, the demonstrated low background parabolic reflectors are a promising platform for low temperature and free-space experiments with NV centers in diamond. Low temperature measurements with these reflectors are underway. Additionally, a new sample (Figure 1-8) with higher aspect ratios has been prepared and is being characterized. With the new sample and technical improvements, the enhanced collection efficiency could potentially improve spin readout fidelity and provide an order-of-magnitude increase in spin-spin entanglement generation rates.

Chapter 2

Diamond nanophotonic and quantum optical devices

The current entanglement rate between two NV centers is 0.004 Hz [38], which is 500 times slower than the spin decoherence rate of ~2 Hz. The results from the previous chapter demonstrate 10× and 3× enhancement in photon flux over that from a single NV located in a unpatterned bulk diamond and solid immersion lens (SILs), respectively. As the spin-spin entanglement rate scales with the square of the collection efficiency, the entanglement rate could already benefit from a 9-fold speedup over experiments using SILs. However, the maximum enhancement in collection efficiency is limited to 25×, which corresponds to a maximal entanglement rate of 0.044 Hz – still 45× below the spin decoherence rate. Therefore, to entangle, store and manipulate more than 2 qubits for quantum information processsing, the spontaneous emission rate of the zero-phonon-line optical transition must be enhanced. In Chapter 2 and Chapter 3, we describe current efforts to engineer the local density of states using cavity quantum electrodynamics.

2.1 Diamond nanofabrication

Photonic elements require refractive index contrast for light confinement. For example, waveguides are often fabricated on low-index materials and cladded by air

or by low-index dielectrics, and optical resonators like photonic crystal cavities and microdisks are typically suspended on distant pedestals to minimize additional loss channels. These structures can be typically fabricated on thin films on a sacrificial material, which is selectively undercut by an isotropic etch, leaving suspended nanostructures. For silicon and III-V materials like GaAs, high-quality (e.g. single crystalline and small surface RMS roughness) thin films are readily available. Silicon-on-insulator (SOI) heterolayers, for example, have demonstrated some of the best optical and mechanical resonators because of the fabrication techniques optimized for silicon processing in the semiconductor industry. At the moment, such mature technologies are lacking in emerging materials platforms like aluminum nitride (AlN, a wide band gap semiconductor), gallium nitride (GaN, a promising high electron mobility transistor), lithium niobate (LiNbO3, a strongly nonlinear optical material) and diamond.

Since the early 1990s, microwave plasma-enhanced chemical vapor deposition (MPE-CVD) has emerged as the preferred process for synthesizing diamond [9]. The flexibility and control afforded by MPE-CVD have enabled the manufacturing of polycrystalline diamond wafers up to 120 mm in diameter, but optical elements such as ring resonators fabricated from such polycrystalline thin films are lossy because of scattering from grain bounderies [10]. As such, most quantum optical experiments and diamond nanophotonic elements have utilized single-crystal diamonds, which have minimal birefringence [11] and low levels of inpurities. However, diamond processing is difficult with such samples, as they are typically 2 mm x 2 mm x 0.3 mm (but available up to 8 mm x 8 mm x 0.3 mm). Moreover, there is still the outstanding challenge of obtaining high quality single-crystal diamond thin films from such bulk materials.

With limited diamond nanofabrication technologies, many innovative techniques have been demonstrated and much effort has been directed towards the development of diamond etching and diamond thin films on the order of optical wavelengths. In particular, controlled, wet etching of diamond is unavailable because diamond is chemically inert. Extreme etchants such as molten potassium nitrate and other

molten metals can etch diamond [12] but they also attack mask materials like oxides, thus incompatible with lithographic processes. As such, diamond is typically processed mechanically or by plasma etching.

Mechanical polishing is unsuitable because it creates strain, which creates local electric fields that Stark shifts optical transitions of NV centers (SiV and GeV centers are less susceptible due to their inversion symmetry and hence vanishing first order electric dipole moment) in diamond. However, mechanical polishing is often used in conjuction with plasma etching, where bulk diamonds are first thinned down to 20 - 50 μm plates and the damanged layers are removed by a subsequent gentle plasma etch.

The most popular platform for producing single-crystal diamond photonic devices is the diamond heterolayer that is inspired by SOI techniques. One such approach relies on crystal ion slicing, where highly directional helium ions create a damaged graphite layer that can be selectively removed using an electrochemical etch[13, 14]. By controlling the bombardment energy, different diamond membrane thicknesses can be realized. However, ion bombardment creates crystal damage, strain and other crystal defects. In another approach, a reactive ion etching (RIE) process thins down a polished 20 - 50 μm diamond to $\sim$ 200 nm. Then, electron beam lithography (EBL) and another RIE process transfer device patterns into the thin film diamond, which is subsequently undercut. This process has been shown to realize photonic crystal (PhC) nanobeam cavities [15, 16], planar PhC cavities [17], microring resonators [18] and micromechanical cantilevers [19, 20, 21]. However, these films are often not homogeneous and have thickness variations up to 300 nm because RIE transfers the wedge profile of the initial diamond plates (a result of polishing) into the final thin film. Moreover, such films are notoriously difficult to manipulate and are often incompatible with the cleaning (boiling acids) and annealing (high temperature) processes involved in nitrogen implantation and nanostructure fabrication.

Recently, a process has combined two of the approches above - crystal ion slicing with RIE thinning - with homoepitaxial overgrowth to create high quality single-crystal diamond thin films that are fused to millimeter-scale diamond frames [22].

While technically challenging, such approaches and variations thereof could be promising especially when considered in volume production, pending further investigation into the NV spectral and spin properties.

Another approach relies on direct three-dimensional micromachining in the form of focused ion beam (FIB) milling. Such approaches have produced triangular nanobeam photonic crystal cavities [23]; however, gallium ions also create crystal damage and mask sputtering that is detrimental to the performance of such devices. Analogous to the FIB milling, recently an RIE-based angled etching process [24] has also demonstrated free-standing structures [25, 26, 27, 28, 29] in a bulk diamond platform. An angled, directional etch is achieved by enclosing the sample in a machined Faraday cage, which is loaded into standard inductively coupled plasma RIE (ICP-RIE) chambers. Because the cage geometry determines the etch angle, this method does not require modifications to ICP-RIE tools, increasing the toolbox of the already indispensable ICP-RIE in diamond nanofabrication.

An interesting proposal could circumvent diamond thin films altogether by engineering the effective index of diamond nanostructures [30]. Such an approach achieves light confinement by cladding a fin structure in lower index materials and could be useful for all-diamond (or similarly challenging materials) photonic circuits. For the specific applications to color centers, however, high-aspect-ratio structures in diamond are difficult to fabricate and the embedded color centers are known to suffer from spectral diffusion due to its proximity to surfaces. Nevertheless, as demonstrated above, there still exists opportunities for developing novel processing techniques that are favorable to the quality of the optical devices and also the spectral and spin properties of NV and other color centers in diamond.

Our recent efforts into a scalable creation of spin-photon interfaces such as optical resonators and microwaveguides will be discussed in the following section. Our work involves fashioning nano- and micro-photonic structures directly from bulk diamond using recent advances in diamond plasma undercutting.

2.2 A quasi-isotropic etching process for suspended diamond nanostructure

Until homogeneous thin films can be scalably produced, a bulk diamond approach to photonic structures is preferred. Additionally, as discussed above, the processing steps of diamond thin films are especially challenging if not incompatible with many of the cleaning and annealing processes involved. Recently, inspired by a similar process for bulk silicon[31], there is a significant development in diamond isotropic etching. Adapted for diamond, this technique has enabled all-diamond microdisk resonators [33] and suspended nanobeam waveguides [32].

A similar process for the fabrication of a variety of photonic structures has been developed. The development of this fabrication process constitutes a substantial part of the work involved in this thesis, and the process is outlined in Figure 2-1. Our main investigation and fabrication results are summarized in the next three subsections.

2.2.1 Sample preparation: Step 0

Nanostructures are typically patterned on high-purity Type IIA single-crystal CVD diamonds with [N]$<$ 1 ppm and 5 ppb, respectively with 100-oriented faces. The as-received diamonds have root-mean-square (RMS) surface roughnesss of $<$ 10 nm, which is on the same order as $\lambda/10$ where λ is the in-material wavelength ($\sim$ 260 nm). Therefore, the diamond must first be polished to reduce optical losses from scattering. Following scaife polishing, the diamond is cleaned in a boiling 1:1:1 mixture of sulfuric, nitric and perchloric acid to remove any graphitized layer. The samples are subsequently chemically polished in a mixture of argon-chlorine (Ar-Cl) plasma to remove the damaged layers from scaife polishing. This is followed by a second polishing step involving oxygen plasma, as Cl etching has been observed to be detrimental to the spin coherence of the NV center. The final RMS surface roughness is $<$ 0.5 nm as verified by atomic force microscopy (AFM). Following nitrogen implantation and annealing for vacancy diffusion and NV formation, the samples are cleaned in

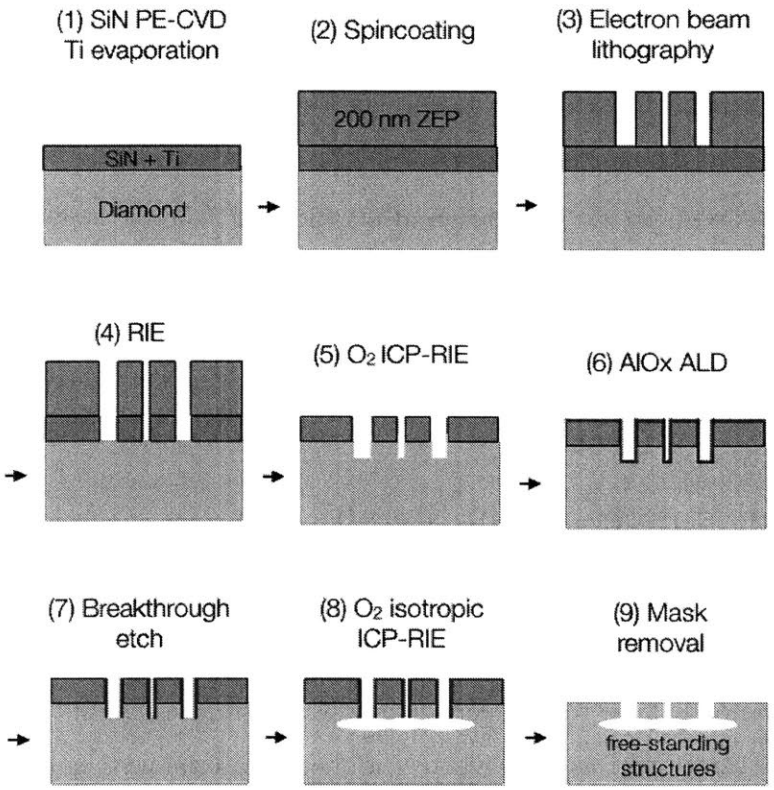

Figure 2-1: Process flow for creating free-standing membranes and photonic structures in diamond. Quasi-isotropic etching releases the structures from the bulk material.

piranha (3:1 mixture of sulfuric acid and hydrogen peroxide) at room temperature to etch residual organics and contaminants from the annealing process.

2.2.2 Electron beam lithography: Step 1-3

A hard mask of silicon nitride (SiN) is deposited on diamond via plasma-enhanced CVD (PE-CVD) using the STS-CVD tool in the Technology Research Laboratories (TRL). This hard mask is needed because diamond can only be etched by oxygen plasma, which strips most resists. A set of alternating RF frequencies is used during the growth process to produce a low-stress 200 nm film of SiN. A 5-nm layer of titanium (Ti) electron-beam discharge layer is then evaporated in the NanoStructures Laboratory (NSL). A positive-tone electron-beam resist, GL2000-11, is spincoated at a speed of 6000 rotations per minute for 60 seconds and then pre-baked at 180°C. Optionally, in place of Ti evaporation, a conductive polymer (e-spacer) can also be spin-coated after resist application.

The GL2000-11 resist is exposed using 125 kV electron beam writer (Elionix F-125) at a nominal dose of 400-800 $\mu C/cm^2$, depending on the chosen developing condition. The exposed areas are removed by o-xylene and development is terminated by an isopropyl alcohol (IPA) soak.

2.2.3 Diamond patterning: Step 4-5

The lithographically defined patterns are transferred into the SiN mask by a reactive ion etch (RIE) process using a plasma chemistry. A fluorine-based chemistry, tetrafluoromethane (CF_4), is used to etch the Ti and SiN layers. The chip is then soaked in hot n-methyl pyrrolidinone (NMP or 1165 developer) at 75°C for 2 hours to strip the residual resist.

The SiN patterns are transferred into diamond using an *an*isotropic (highly directional) ICP reactive ion etcher with the following process parameters: 32°C, 0.2 mTorr pressure, 500 W ICP power and 240 W bias power. This step defines the thickness of the 'membrane' or photonic structures.

2.2.4 Isotropic etch: Step 6-9

Next, the sample is conformally coated with aluminum oxide (Al_2O_3) via atomic layer deposition (ALD) using the Cambridge Nanotech tool in the Exploratory Materials Laboratory (EML). A short anisotropic RIE using CF_4 is then used to break through the Al_2O_3 layer, after which oxygen plasma at zero-bias and 900 W ICP power is used to isotropically etch unprotected diamond surfaces at 200°C. Critically, this selective removal undercuts the diamond photonic structures because their sidewalls remain protected by Al_2O_3. Finally, the SiN and Al_2O_3 mask layers are stripped in concentrated hydrofluoric acid and the diamond is supercritically dried for higher device yield.

The timing of this etch is critical for the final thickness of the structure. A set of cantilevers with increasing widths, as shown in Fig 3-2a is included in the pattern to study the etch rates, as the etch rate is nonlinear and dependent on the width of the structure[33]. The surface of the isotropically etched diamond mirrors the bottom of the masked structure, as shown in Figure 3-2b. This shape is due to the different etch rates of different crystal planes; etch rates along the 100 and 111 crystal planes add up near the base while the inward etch rate is slower in that direction by virtue of having less etchable surface area. A tungsten probe is used to detach and flip the cantilevers (Fig. 3-2c). As expected, only the narrowest cantilever has a flat bottom surface. Therefore, this observation can be used as the signal of uniform and complete undercutting.

Single-mode microwaveguides and photonic crystal nanobeam cavities have been successfully fabricated using this approach. The results are described in Chapter 3.

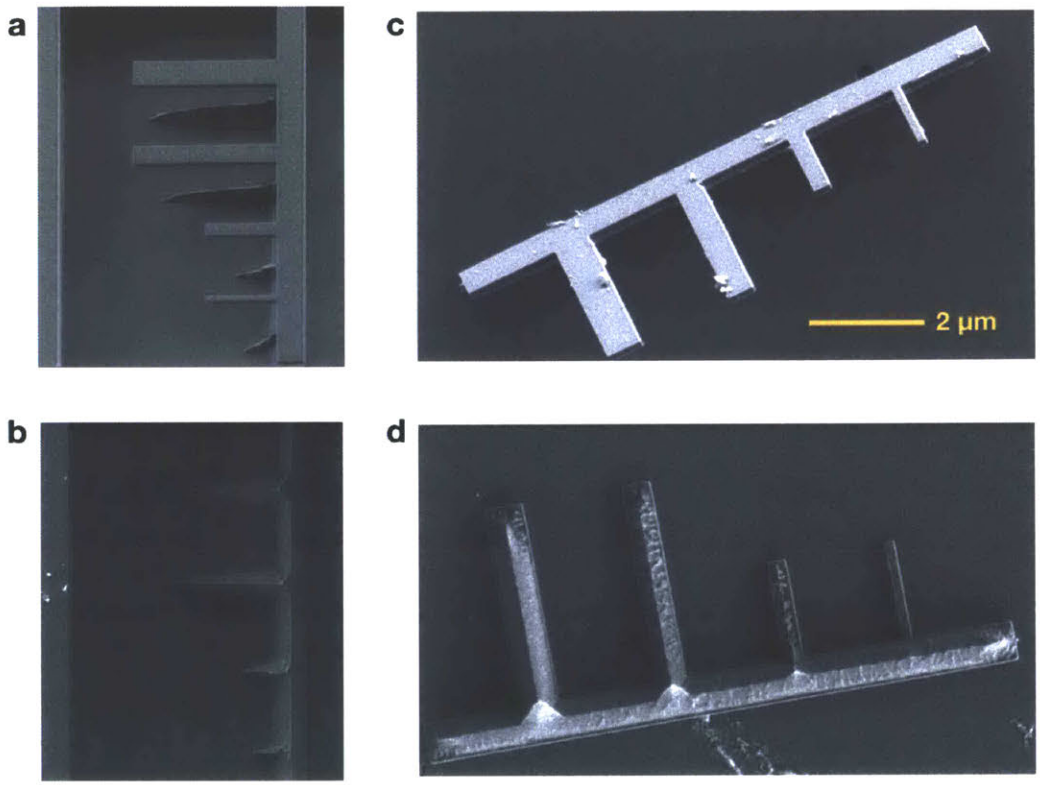

Figure 2-2: (a)Scanning electron micrograph of cantilevers with varying widths fabricated with quasi-isotropic etching. (b) The cantilevers are removed using a micro-manipulator. (c) Using the same micro-manipulator, the cantilevers are transferred onto the surface of the bulk diamond for imaging. (d) The cantilevers are flipped to reveal and verify the flatness of their bottom surfaces. As expected, only the narrowest cantilever has a flat surface(cf Fig.(b))

Chapter 3

Enhancing NV-photon interaction

The rapid progress in nanophotonics has enabled researchers to engineer light-matter interactions in solid-state materials to strengths that had only be seen in atomic physics. In 1946, Edward Purcell realized that an emitter's radiative rates are not intrinsic properties but they depend on the emitter's coupling with the environment [34]. The field of cavity quantum electrodynamics (cavity QED) quickly developed within atomic physics, and with recent advances in nanofabrication in the past two decades, strong light-matter interactions have also been observed in semiconductor QED systems.

3.1 Waveguide and cavity quantum electrodynamics

Photonic crystals (PhC) are among the most popular and powerful platforms for solid-state QED. The periodicity and symmetry of the dielectric constants in a PhC add functionality to the bulk material through interference and Bragg scattering[35]. The allowed modes in such a structure are the so-called optical Bloch modes, in direct analogy to the electronic Bloch modes. Similar to semiconductors, a photonic bandgap can open in a PhC, enabling control of the allowed modes and frequencies. Such bandgaps can also exist in one-dimensional and two-dimensional PhC, where refractive index contrast provides the confinement in the out-of-plane directions.

Importantly, the local density of states (LDOS) can be modified using a PhC,

allowing the enhancement or suppression of dipole transition rates. Additionally, by introducing lattice defects to break the symmetry of the crystal structure, cavity modes may appear in the bandgap. An emitter coupled to a cavity mode can therefore form an efficient optical interface.

The LDOS (in the Markov approximation) is given by

$$\rho(\mathbf{r}, \omega, \hat{\mathbf{e}}_\mathbf{d}) = \frac{n\omega^2}{3\pi^2 c^3} F_p(\mathbf{r}, \omega, \hat{\mathbf{e}}_\mathbf{d}) \tag{3.1}$$

where

$$F_p(\mathbf{r}, \omega, \hat{\mathbf{e}}_\mathbf{d}) = \frac{\gamma_{\text{rad}}(\mathbf{r}, \omega, \hat{\mathbf{e}}_\mathbf{d})}{\gamma_{\text{rad}}^{\text{hom}}(\omega)} \tag{3.2}$$

is the ratio of the radiative decay rate of the emitter at $\mathbf{r}$ to that in a homogeneous medium, n is the refractive index of the homogeneous medium and $\hat{e}_d$ is the polarization unit vector of the dipole emitter [36]. Also known as the Purcell factor, it describes the suppression ($F_p < 1$) or enhancement ($F_p > 1$) of spontaneous emission. Moreover, F_p can be experimentally determined by lifetime measurements. In the next few sections, we will describe the design and fabrication of structures that enhance the interaction strength between light and spin qubits such as NV centers.

3.2 Quantum memory nodes

As opposed to optical cavities, dielectric waveguides tend to exhibit modest Purcell effects. However, they are also broadband and can be very efficient, making them promising interfaces between NV centers and photons. The efficiency of such interfaces can be described by

$$\beta = \frac{\Gamma_{\text{wg}}}{\Gamma_{\text{wg}} + \Gamma_{\text{ng}} + \Gamma_{\text{nr}}} \tag{3.3}$$

where Γ_{wg}, Γ_{ng} and Γ_{nr} are the decay rate into the (single) waveguide mode, non-guided modes and non-radiative modes, respectively. Moreover, they are more robust to misalignment and fabrication imperfections due to their non-resonant nature and

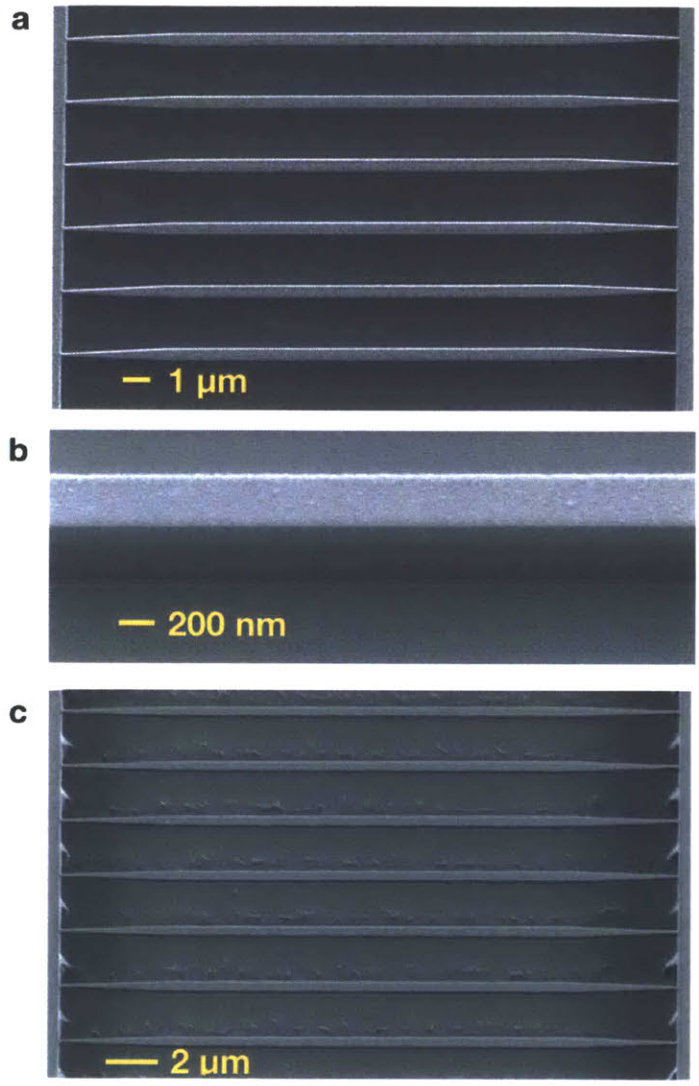

Figure 3-1: (a) Scanning electron micrograph of the SiN hard mask and nanowires in bulk diamond. (b) An optimized inductively coupled plasma reactive ion etching (ICP-RIE) transfers the SiN pattern into the diamond. (c) A quasi-isotropic process (Fig.2-1) is used to release the nanowires.

larger mode volumes.

NV centers located in such a single-mode waveguide can have $\beta = 0.86$, allowing an efficient readout of NV ZPL and sideband photons [37]. The photons from these "quantum nodes" can also be directly coupled into a photonic integrated circuits (PIC) for on-chip filtering, routing and interference. As demonstrated in a silicon nitride (SiN) PIC, up to 96% of the NV fluorescence can be coupled into the SiN waveguide mode by engineering an adiabatic mode transition at the diamond-SiN interface [37, 2]. In this section, this work is extended using the fabrication techniques introduced in Chapter 2. In particular, structures with higher β for NV and other color centers are fabricated to be integrated into PICs that are concurrently being developed in our group as well.

The fabrication process of these micro waveguides is shown in Figure 3-1. The SiN hard mask and nanowires are shown in the scanning electron micrograph in Figure 3-1a. The SiN mask pattern is transferred into diamond with a high etch selectivity of 33 (Fig.3-1b) using an optimized inductively coupled plasma RIE (ICP-RIE). The structures are released by undercutting the nanowires in a well-timed quasi-isotropic process as described in Chapter 2. The waveguides can then be transferred and aligned to an AlN waveguide with nanometer precision using a micro-manipulator. Therefore, by post-selecting only the highest quality of quantum nodes, basic on-chip quantum networks with photonic routing, integrated lasers, and single photon detection can be assembled. The prospects of this hybrid platform is described in Chapter 4.

Whereas the diamond nanowire exhibits modest Purcell enhancements and high β factors, the ZPL photon generation rate would need to be significantly enhanced to overcome the spin decoherence rate. This is especially challenging for NV centers, where the coherent ZPL photons only comprise about 3-4% of the total photon emission. To entangle two remote NV electron spins, the success probability scales with the square of the ZPL detection efficiency. With the current highest entanglement rate of 0.004 Hz between two NV centers [38], it is unrealistic to entangle n >2 qubits over a quantum network. Thus, it is necessary to achieve high F_p at ω_{ZPL}. In the

next section, we describe our effort towards nanoscale optical cavities in diamond.

3.3 Photonic crystal cavities

When the cavity decay rate $\Gamma_{\text{cav}} \gg \Gamma_{\text{ng}}$, the Purcell factor is given by

$$F_P^{\text{cav}}(\mathbf{r}, \Delta, \hat{\mathbf{e}}_\mathbf{d}) = F_P^{\max} f(\mathbf{r}) |\hat{e}_d \cdot \hat{e}_{\text{cav}}^*| \frac{\omega_{\text{cav}}^2/4Q^2}{\Delta^2 + \omega_{\text{cav}}^2/4Q^2} \tag{3.4}$$

where ω_{cav} is the cavity frequency, $\Delta = \omega_{\text{cav}} - \omega$, $\hat{e}_{\text{cav}}$ is the polarization unit vector of the cavity mode, Q is the cavity quality factor and

$$F_P^{\max} = \frac{3(\lambda/n)^3}{4\pi^2} \frac{Q}{V_{\text{eff}}} \tag{3.5}$$

$$V_{\text{eff}} = \frac{1}{\max[\epsilon(\mathbf{r})|\mathbf{u}_{\text{cav}(\mathbf{r})}|^2]} \tag{3.6}$$

$$f(\mathbf{r}) = \frac{\epsilon(\mathbf{r})|\mathbf{u}_{\text{cav}}(\mathbf{r})|^2}{\max[\epsilon(\mathbf{r})|\mathbf{u}_{\text{cav}(\mathbf{r})}|^2]} \tag{3.7}$$

In particular, $\mathbf{u}_{\text{cav}}$ is the cavity mode, V_{eff} describes the effective mode volume and $f(\mathbf{r})$ describes the spatial and polarization alignment between the dipole emitter and cavity field. In the ideal case of perfect alignment and zero detuning, equation 3.5 reduces to

$$F = F_P^{\max} = \frac{3(\lambda/n)^3}{4\pi^2} \frac{Q}{V_{\text{eff}}} \tag{3.8}$$

The quality factors are determined from the photoluminescence spectra as shown in Figure 3-4(b). Quality factors exceeding 15,000 and an average Q of ~3,000 are inferred from Figure 3-4(b-c). Across an array of cavities with identical parameters, the spread in cavity resonances is $\Delta\lambda < 5$ nm, well within the range of cavity tuning. Compared to the membrane approach to diamond photonic devices, this fabrication process is therefore repeatable and reliable, which is important for scalability of NV-based quantum memories.

The next chapter outlines our effort towards the construction of a quantum computer based on diamond spin qubits.

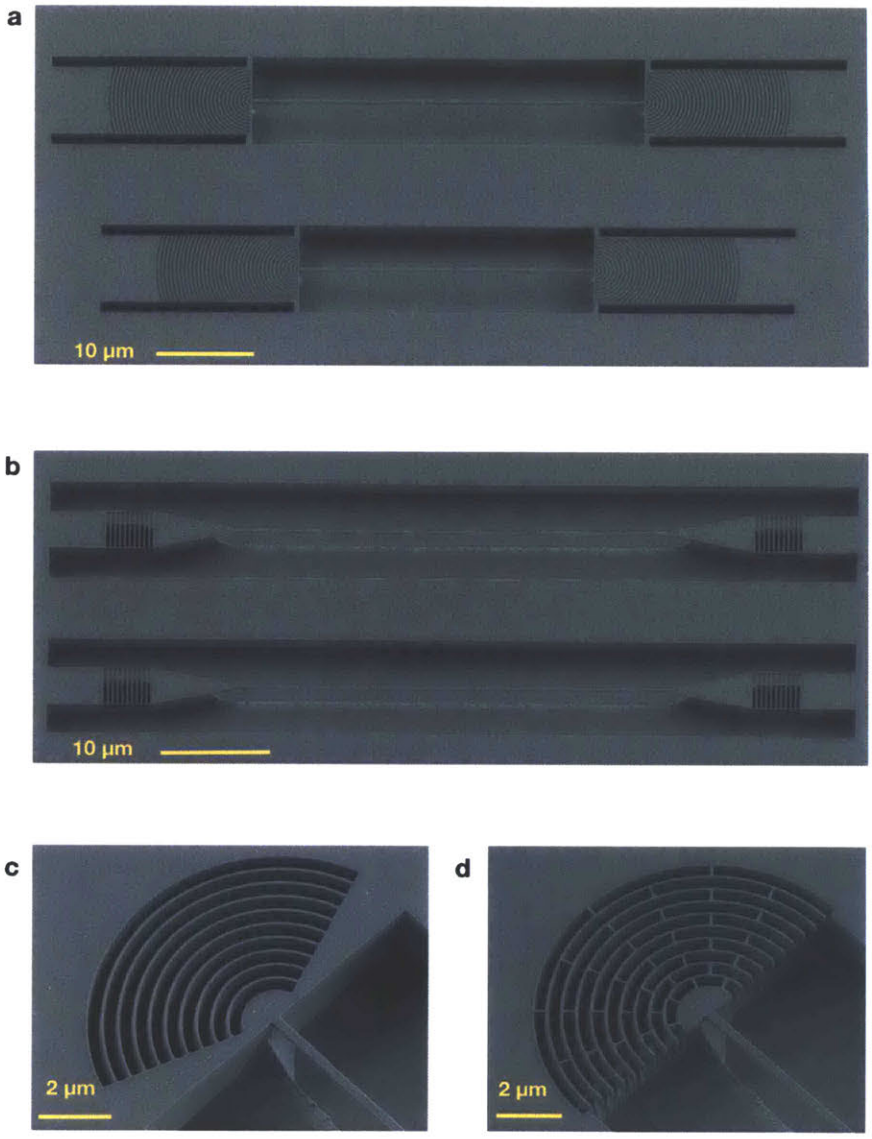

Figure 3-2: The quasi-isotropic process (Fig.2-1) can also be used to undercut complex geometries such as grating couplers and potentially two-dimensional planar photonic crystal cavities. Such waveguides can also be readily used for to enhance photon-SiV and photon-GeV centers in diamond.

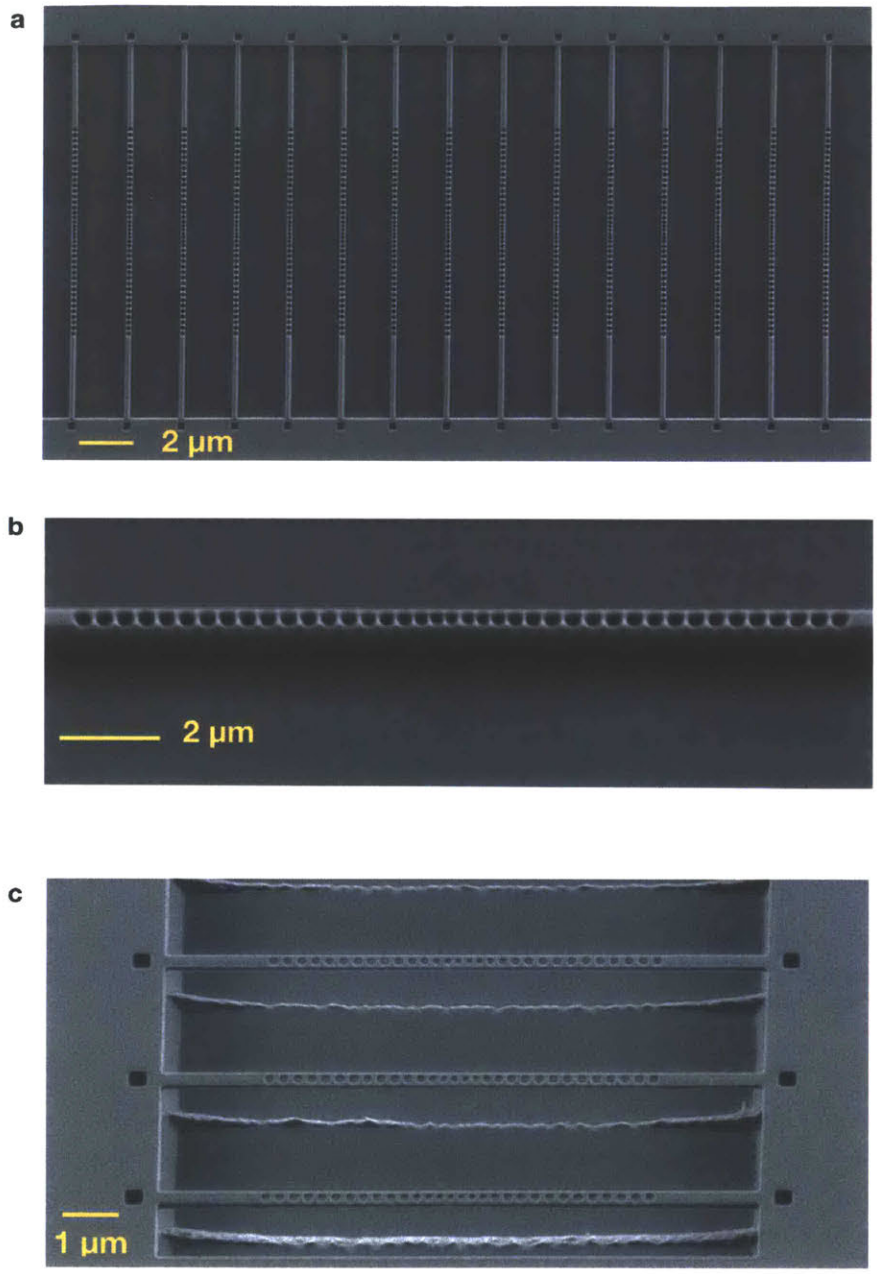

Figure 3-3: (a) Scanning electron micrograph of the SiN hard mask and photonic crystal (PhC) nanobeam cavities in bulk diamond. (b) An optimized inductively coupled plasma reactive ion etching (ICP-RIE) transfers the SiN pattern into the diamond. (c) A quasi-isotropic process (Fig.2-1) is used to release the PhC nanobeam cavities.

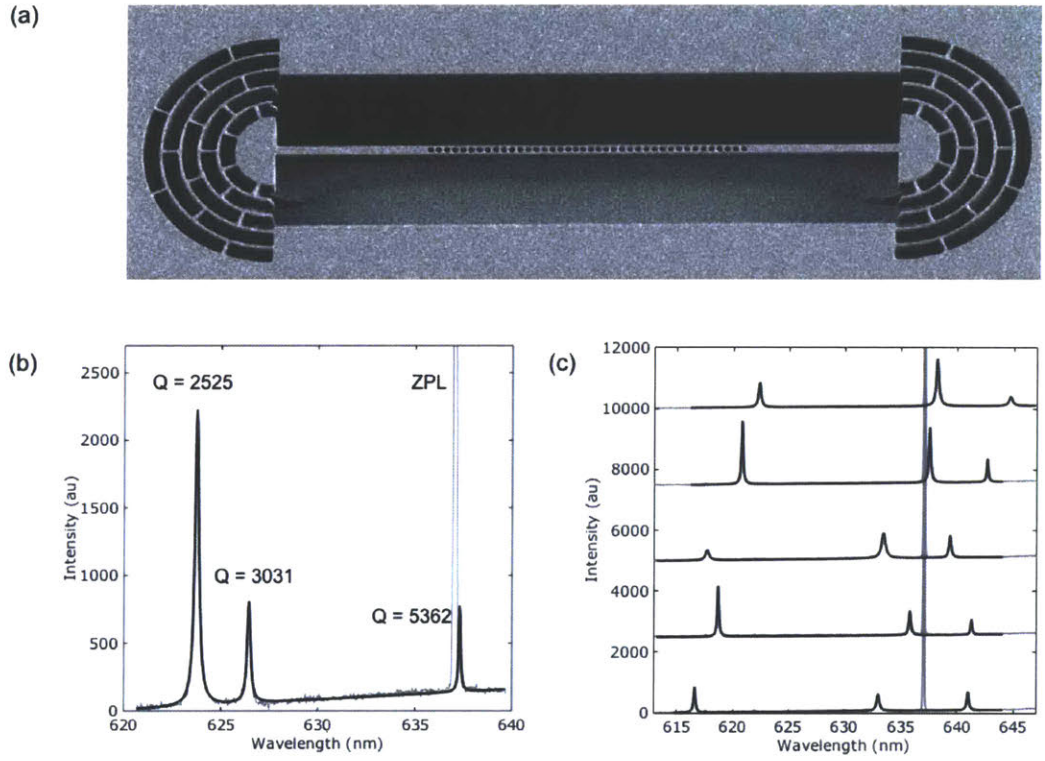

Figure 3-4: (a) Scanning electron micrograph of a photonic crystal (PhC) nanobeam cavity in bulk diamond. (b) Quality factors of one of the fabricated PhC cavity, showing a cavity mode near the ZPL with $Q = 5362$ at $\lambda = 637.3$ nm. (c) Distribution of cavity resonances of a PhC cavity with identical cavity a and r parameters.

Chapter 4

Towards scalable creation of quantum memories

As discussed in Equation 3.5, the maximum Purcell enhancement is achieved when the emitter is perfectly aligned with the cavity field maximum. Therefore, it is important that the NV center be placed deterministically at the cavity field maximum. Alternatively, the nano-cavity may be placed over the NV center. In general, there are three approaches towards coupling NV centers with nanophotonic structures.

1. *Post-selection.* Many photonic structures are fabricated at once across a diamond sample that has implanted or natural NVs. The sample is screened using fluorescence and confocal microscopy for coincidental NVs in photonic structures. This approach is generally taken to study semiconductor quantum optics with solid-state qubits such as quantum dots and defect centers, and it is the approach taken by e.g. references [17, 16, 6, 39]. However, this method has inherently very low yield, and there is no known process towards scalable quantum networks using this approach.

2. *Targeted implantation.* Photonic structures are first fabricated and color centers are created at the desired locations using an aperture or a focused ion beam. This approach could potentially reduce the amount of characterization experiments. However, the yield is also low in this process due to the stochastic nature

of NV formation. Silicon vacancy (SiV) and germanium vacancy (GeV) centers are promising defect centers in diamond that benefit from this approach due to the availability of focused ion beams for Si and Ge [40, 41]. Still, current yield levels at ~1% (NV centers) and ~2.5% (SiV and GeV centers) preclude this approach from generating multi-NV networks beyond 3 qubits.

3. *Registration.* Alignment markers are defined on the sample following NV implantation. The sample is then screened using fluorescence and confocal microscopy. The problem of stochastic creation of color centers is overcome by fabricating photonic structures relative to registered color centers. This approach has a high yield of NV-coupled structures, and it is the approach taken by e.g. references [7, 42]. The final yield is completely determined by the fabrication process. The ability to control the yield is very important for the scalable creation of cavity-coupled NV centers, as described in the next sections.

4.1 A high-yield hybrid network for quantum memories based on NV centers

In addition to high-fidelity quantum gates, implementing truly scalable quantum networks would require a robust optical interface and network for transmitting, manipulating and mapping photonic quantum states.

As discussed, processes with low yield are not scalable as the number of fabrication cycles grows exponentially with the number of entangled qubits. Equally important, the experimental overhead (number of lasers and 'which-path-eraser' networks) also grows with the size of the network; it is unlikely for current free-space diamond experiments to scale beyond 10 entangled qubits. However, demonstrating quantum supremacy and implementing meaningful quantum algorithms would require at least 50 qubits [43].

The scaling is less daunting in a photonic integrated circuit (PIC) platform: the interferometers have phase stability, optical nodes have low loss and sources can be

on- or off- chip. Implementing such networks directly on diamond, however, would again be limited by the quantum node yield.

In our approach, the fabrication of the quantum node (diamond waveguide or nano-cavity) is decoupled from the the fabrication of the optical network (Aluminum nitride PIC). This hybrid platform allows the integration of pre-characterized, high quality diamond nodes into a separate chip comprising the photonic backbone of the network.

A bulk diamond approach along with quasi-undercutting has been developed in order to post-select only the best diamond nodes for integration with the PIC (Chapter 2 and Chapter 3). Upon successful verification and characterization, diamond nodes containing single NV with excellent optical properties are detached from their parent crystal and coupled directly with the PIC [37].

An entire diamond chip ($\sim$3 mm x 3 mm) is characterized in a purpose-built automatic microscope. Deterministic fabrication with high nanostructure-coupled NV yield is then possible. Our effort towards this direction is briefly described in the rest of this chapter.

Alignment marks are first etched into the diamond to enable optical localization of NV centers using a widefield microscope. A typical GDS of our diamond coordinate system is shown in Figure 4-1(a). Global alignment marks (circled in red) for subsequent electron beam lithography (EBL) steps are circled in red, and the coordinate on the diamond is represented by Figure 4-1(c). The coordinates are encoded in the 2D array of bits in Figure 4-1(c,d).

During the screening step, NV centers are determined by their fluorescence and confirmed by electron spin resonance. NV centers are localized relative to the 4 coordinate markers within the field of view. Their coordinates relative to the markers are stored and used as the input in the generation of the next GDS.

The fabrication process is described by Figure 4-1(e). First, a hard mask of SiN is deposited. Then, a positive-tone electron beam resist is spincoated. The hard mask is defined by electron beam lithography and reactive-ion etching (RIE), and pattern transfer is achieved by inductively coupled plasma reactive-ion etching (ICP-RIE).

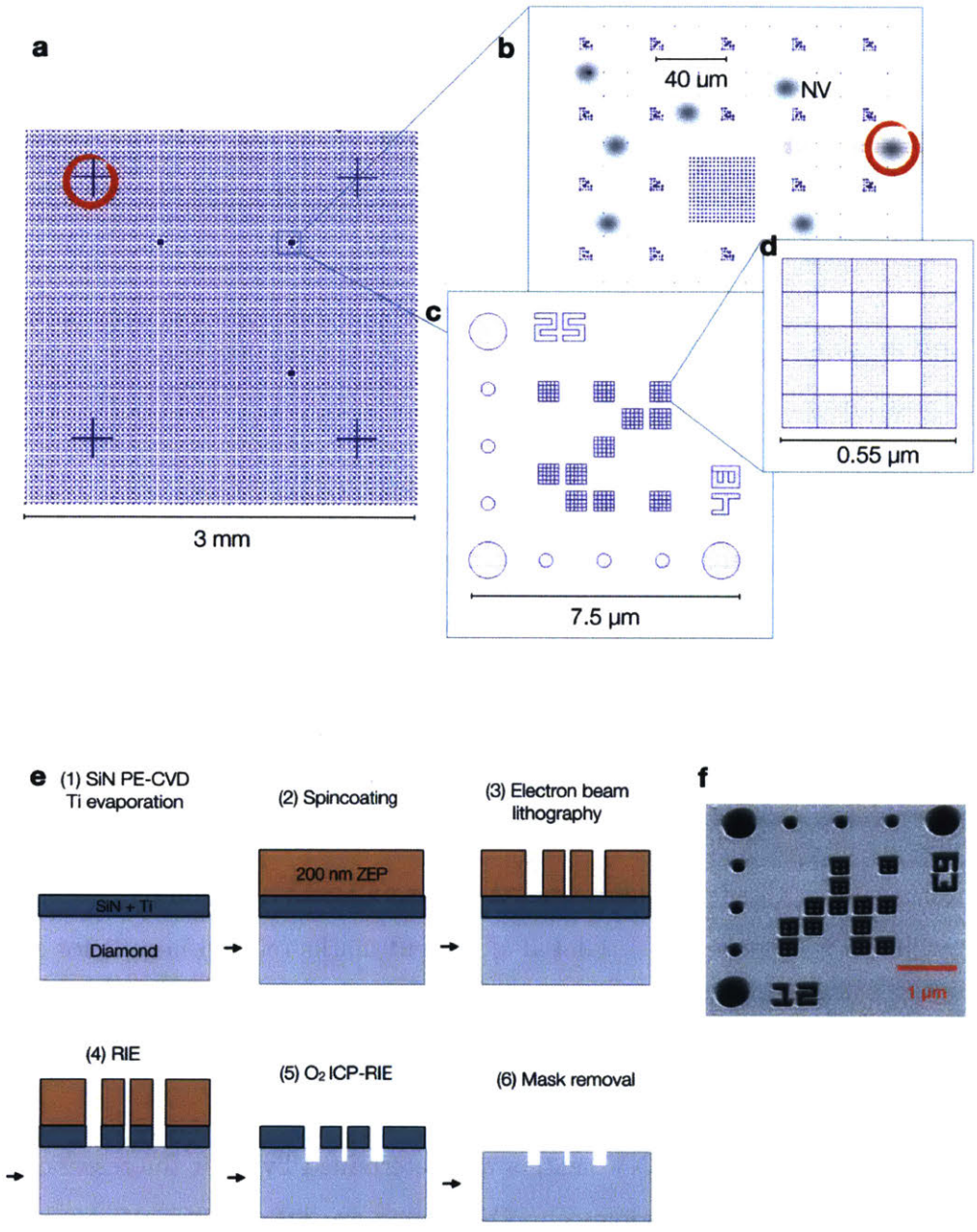

Figure 4-1: (a)-(d). Coordinate system used for localization and registration of NV centers. (e) Process flow of the fabrication of the coordinate system. (f) Scanning electron micrograph of an individual coordinate marker.

The mask is wet etched using hydrofluoric acid, after which the diamond is cleaned in a 3:1 mixture of sulfuric acid and hydrogen peroxide.

After the localization experiment, photonic and mesa structures are aligned over the registered NV centers with high precision using electron beam lithography (EBL). To evaluate the fidelity of the alignment process, mesa structures A and B (see GDS in Figure 4-2(b)) are written relative to the existing first layer (Figure 4-2(a)). Aligned lithography is performed using two methods: "manual" overlay and "automatic" overlay. Manual overlay is the conventional method used in multi-layer EBL, where the global alignment markers are identified by the user in SEM mode.

The result of this aligned lithography is shown in Figure 4-2(c). The GDS of the mesa structures is overlaid over the micrograph in Figure 4-2(e), showing signifcant displacement. The displacement is quantified in Figure 4-3(a-b): near the center of the diamond chip ("cavity region"), the displacement error is 123.8 ± 21.2 nm and 131.2 ± 10.7 nm for structure A and B, respectively.

The accuracy can be improved using an "automatic" overlay procedure, where edge detection and linescans are used to determine the coordinates of the alignment marks. The result of this procedure is shown in Figure 4-2(d-e). The displacement errors are 27.7 ± 8.7 nm and 26.2 ± 7.0 nm for structure A and B, respectively (Figure 4-3(a-b)), demonstrating a significant improvement in alignment accuracy.

More importantly, an alignment accuracy of $\sigma < 40$ nm places us within the tolerance limit of the photonic crystal nanobeam cavities presented in Chapter 4. At this emitter displacement, the Purcell factor, F_p would be within 50% of $F_{p,max}$. Using this systematic fabrication, with $\sigma = 40$ nm and $N = 2,500$ fabricated cavities per chip, about $\sim$4% or $N_{enhanced} = 95$ of the registered NV centers would be within $\pm$ 10 nm from the cavity field maximum. Integrating such a large number of nanocavity-enhanced single NV centers (Chapter 3) with photonic integrated circuits is being actively pursued.

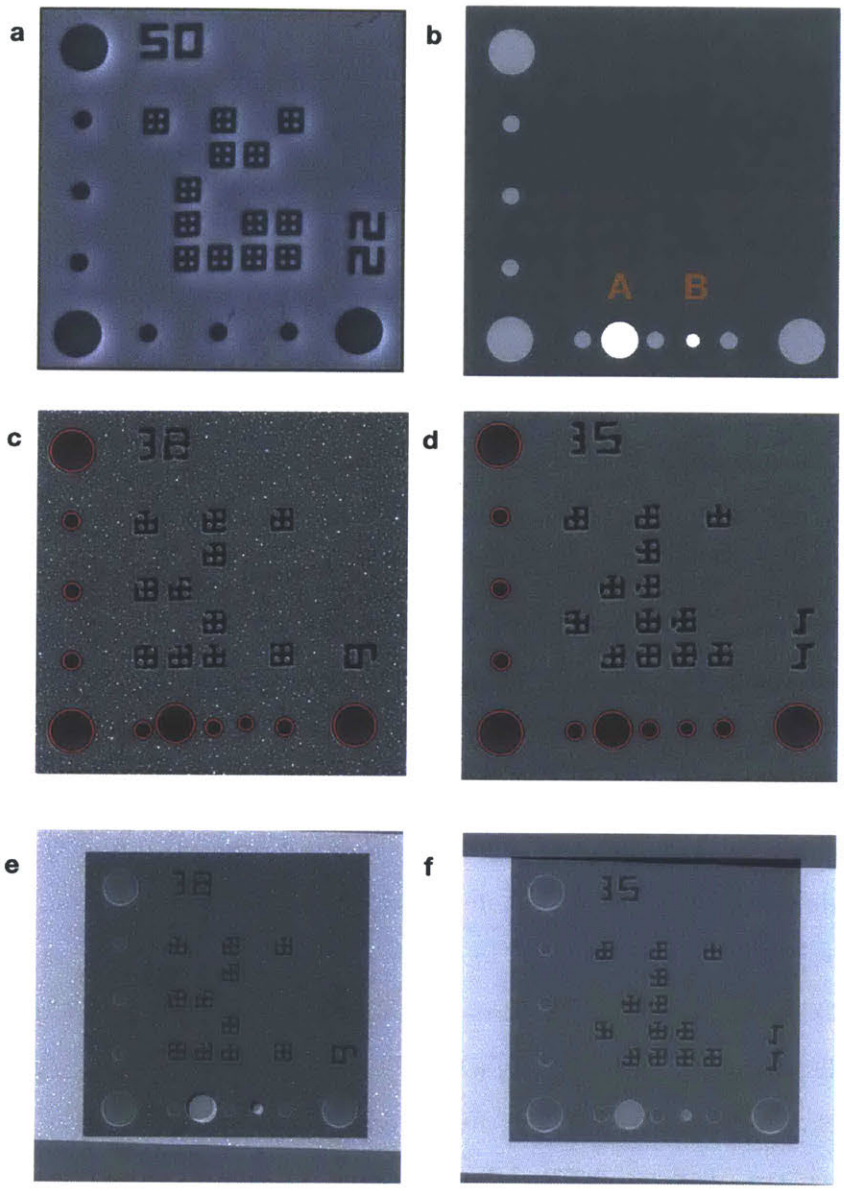

Figure 4-2: (a) First layer and (b) second layer of the GDS design. A and B are mesa structures that are etched into the diamond to evalute the alignment accuracy. (c) Result of the overlay experiment using "manual" mode (see main text). (d) Result of the overlay experiment using "automatic" mode. The superimposition of GDS and SEM images are shown in (e) and (f) for "manual" and "automatic" methods, respectively.

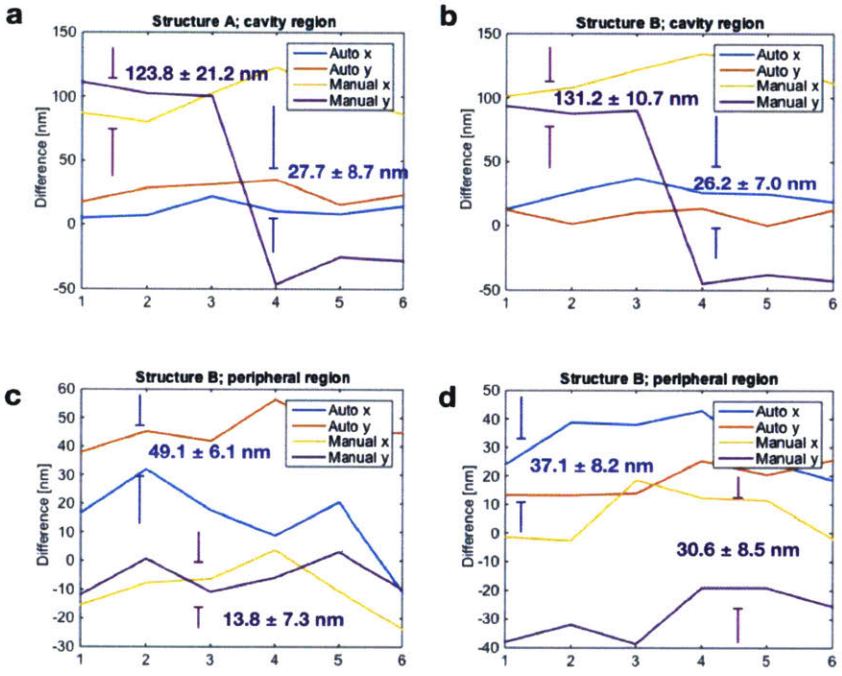

Figure 4-3: Displacement errors of structures A and B. "Cavity" region denotes the center of the diamond, whereas "peripheral" region denotes the area outside the global alignment marks.

Bibliography

[1] Tim Schröder, Sara L Mouradian, Jiabao Zheng, Matthew E Trusheim, Michael Walsh, Edward H Chen, Luozhou Li, Igal Bayn, and Dirk Englund. Quantum nanophotonics in diamond [invited]. *JOSA B*, 33(4):B65–B83, 2016.

[2] Sara Mouradian, Tim Schröder, Jiabao Zheng, Tsung-Ju Lu, Hyeongrak Choi, Noel Wan, Michael Walsh, Eric Bersin, and Dirk Englund. Nv-based quantum memories coupled to photonic integrated circuits. In *SPIE Nanoscience+ Engineering*, pages 992014–992014. International Society for Optics and Photonics, 2016.

[3] Mohammad Jamali, Ilja Gerhardt, Mohammad Rezai, Karsten Frenner, Helmut Fedder, and Jörg Wrachtrup. Microscopic diamond solid-immersion-lenses fabricated around single defect centers by focused ion beam milling. *Review of Scientific Instruments*, 85(12):123703, 2014.

[4] JP Hadden, JP Harrison, AC Stanley-Clarke, L Marseglia, Y-LD Ho, BR Patton, JL O Brien, and JG Rarity. Strongly enhanced photon collection from diamond defect centers under microfabricated integrated solid immersion lenses. *Applied Physics Letters*, 97(24):241901, 2010.

[5] Y. Chu, N. de Leon, and M. Lukin. Coherent optical transitions in implanted nitrogen vacancy centers. *Nano Letters*, 14:1982–1986, March 2014.

[6] Luozhou Li, Edward H Chen, Jiabao Zheng, Sara L Mouradian, Florian Dolde, Tim SchroÌĹder, Sinan Karaveli, Matthew L Markham, Daniel J Twitchen, and Dirk Englund. Efficient photon collection from a nitrogen vacancy center in a circular bullseye grating. *Nano letters*, 15(3):1493–1497, 2015.

[7] Lucio Robledo, Lilian Childress, Hannes Bernien, Bas Hensen, Paul FA Alkemade, and Ronald Hanson. High-fidelity projective read-out of a solid-state spin quantum register. *Nature*, 477(7366):574–578, 2011.

[8] Hannes Bernien, Bas Hensen, Wolfgang Pfaff, Gerwin Koolstra, MS Blok, Lucio Robledo, TH Taminiau, Matthew Markham, DJ Twitchen, Lilian Childress, et al. Heralded entanglement between solid-state qubits separated by three metres. *Nature*, 497(7447):86–90, 2013.

[9] Element Six. The element six cvd diamond handbook.

[10] P Rath, N Gruhler, S Khasminskaya, C Nebel, C Wild, and WHP Pernice. Waferscale nanophotonic circuits made from diamond-on-insulator substrates. *Optics express*, 21(9):11031–11036, 2013.

[11] ML Markham, JM Dodson, GA Scarsbrook, DJ Twitchen, G Balasubramanian, F Jelezko, and J Wrachtrup. Cvd diamond for spintronics. *Diamond and Related Materials*, 20(2):134–139, 2011.

[12] AJ Neves and Maria Helena Nazaré. *Properties, growth and applications of diamond*. Number 26. IET, 2001.

[13] CF Wang, EL Hu, J Yang, JE Butler, et al. Fabrication of suspended single crystal diamond devices by electrochemical etch. *Journal of Vacuum Science & Technology B*, 25(3):730–733, 2007.

[14] Barbara A Fairchild, Paolo Olivero, Sergey Rubanov, Andrew D Greentree, Felix Waldermann, Robert A Taylor, Ian Walmsley, Jason M Smith, Shane Huntington, Brant C Gibson, et al. Fabrication of ultrathin single-crystal diamond membranes. *Advanced Materials*, 20(24):4793–4798, 2008.

[15] BJM Hausmann, BJ Shields, Q Quan, Y Chu, NP De Leon, R Evans, MJ Burek, AS Zibrov, M Markham, DJ Twitchen, et al. Coupling of nv centers to photonic crystal nanobeams in diamond. *Nano letters*, 13(12):5791–5796, 2013.

[16] L. Li, T. Schroder, E. Chen, M. Walsh, and D. Englund. Coherent spin control of a nanocavity-enhanced qubit in diamond. *Nature Communications*, 6:6173, January 2015.

[17] Andrei Faraon, Charles Santori, Zhihong Huang, Victor M Acosta, and Raymond G Beausoleil. Coupling of nitrogen-vacancy centers to photonic crystal cavities in monocrystalline diamond. *Physical review letters*, 109(3):033604, 2012.

[18] BJM Hausmann, I Bulu, V Venkataraman, P Deotare, and M Lončar. Diamond nonlinear photonics. *Nature Photonics*, 8(5):369–374, 2014.

[19] P Ovartchaiyapong, LMA Pascal, BA Myers, P Lauria, and AC Bleszynski Jayich. High quality factor single-crystal diamond mechanical resonators. *Applied Physics Letters*, 101(16):163505, 2012.

[20] Y Tao, JM Boss, BA Moores, and CL Degen. Single-crystal diamond nanomechanical resonators with quality factors exceeding one million. *Nature communications*, 5, 2014.

[21] Arne Barfuss, Jean Teissier, Elke Neu, Andreas Nunnenkamp, and Patrick Maletinsky. Strong mechanical driving of a single electron spin. *Nature Physics*, 2015.

[22] Afaq H Piracha, Patrik Rath, Kumaravelu Ganesan, Stefan KuÌĹhn, Wolfram HP Pernice, and Steven Prawer. Scalable fabrication of integrated nanophotonic circuits on arrays of thin single crystal diamond membrane windows. *Nano letters*, 16(5):3341–3347, 2016.

[23] Igal Bayn, Boris Meyler, Joseph Salzman, and Rafi Kalish. Triangular nanobeam photonic cavities in single-crystal diamond. *New Journal of Physics*, 13(2):025018, 2011.

[24] Pawel Latawiec, Michael J Burek, Young-Ik Sohn, and Marko Lončar. Faraday cage angled-etching of nanostructures in bulk dielectrics. *Journal of Vacuum Science & Technology B*, 34(4):041801, 2016.

[25] Michael J Burek, Nathalie P de Leon, Brendan J Shields, Birgit JM Hausmann, Yiwen Chu, Qimin Quan, Alexander S Zibrov, Hongkun Park, Mikhail D Lukin, and Marko LoncÌŇar. Free-standing mechanical and photonic nanostructures in single-crystal diamond. *Nano letters*, 12(12):6084–6089, 2012.

[26] Michael J Burek, Yiwen Chu, Madelaine SZ Liddy, Parth Patel, Jake Rochman, Srujan Meesala, Wooyoung Hong, Qimin Quan, Mikhail D Lukin, and Marko Lončar. High quality-factor optical nanocavities in bulk single-crystal diamond. *Nature communications*, 5, 2014.

[27] Srujan Meesala, Young-Ik Sohn, Haig A Atikian, Samuel Kim, Michael J Burek, Jennifer T Choy, and Marko Lončar. Enhanced strain coupling of nitrogen-vacancy spins to nanoscale diamond cantilevers. *Physical Review Applied*, 5(3):034010, 2016.

[28] Michael J Burek, Justin D Cohen, Seán M Meenehan, Thibaud Ruelle, Srujan Meesala, Jake Rochman, Haig A Atikian, Matthew Markham, Daniel J Twitchen, Mikhail D Lukin, et al. Diamond optomechanical crystals. *arXiv preprint arXiv:1512.04166*, 2015.

[29] M Schukraft, J Zheng, T Schröder, SL Mouradian, M Walsh, ME Trusheim, H Bakhru, and DR Englund. Invited article: Precision nanoimplantation of nitrogen vacancy centers into diamond photonic crystal cavities and waveguides. *APL Photonics*, 1(2):020801, 2016.

[30] Richard R Grote and Lee C Bassett. Single-mode optical waveguides on native high-refractive-index substrates. *arXiv preprint arXiv:1601.01239*, 2016.

[31] Kevin A Shaw, Z Lisa Zhang, and Noel C MacDonald. Scream i: a single mask, single-crystal silicon, reactive ion etching process for microelectromechanical structures. *Sensors and Actuators A: Physical*, 40(1):63–70, 1994.

[32] Behzad Khanaliloo, Harishankar Jayakumar, Aaron C Hryciw, David P Lake, Hamidreza Kaviani, and Paul E Barclay. Single-crystal diamond nanobeam waveguide optomechanics. *Physical Review X*, 5(4):041051, 2015.

[33] Behzad Khanaliloo, Matthew Mitchell, Aaron C Hryciw, and Paul E Barclay. High-q/v monolithic diamond microdisks fabricated with quasi-isotropic etching. *Nano letters*, 15(8):5131–5136, 2015.

[34] Edward Mills Purcell. Spontaneous emission probabilities at radio frequencies. *Physical Review*, 69:681, 1946.

[35] J. Joannopoulos, S. Johnson, J. Winn, and R. Meade. *Photonic Cyrstals: Molding the Flow of Light.* Princeton University Press, 2 edition, 2008.

[36] Peter Lodahl, Sahand Mahmoodian, and Søren Stobbe. Interfacing single photons and single quantum dots with photonic nanostructures. *Reviews of Modern Physics*, 87(2):347, 2015.

[37] Sara L Mouradian, Tim Schröder, Carl B Poitras, Luozhou Li, Jordan Goldstein, Edward H Chen, Michael Walsh, Jaime Cardenas, Matthew L Markham, Daniel J Twitchen, et al. Scalable integration of long-lived quantum memories into a photonic circuit. *Physical Review X*, 5(3):031009, 2015.

[38] Wolfgang Pfaff, BJ Hensen, Hannes Bernien, Suzanne B van Dam, Machiel S Blok, Tim H Taminiau, Marijn J Tiggelman, Raymond N Schouten, Matthew Markham, Daniel J Twitchen, et al. Unconditional quantum teleportation between distant solid-state quantum bits. *Science*, 345(6196):532–535, 2014.

[39] Thomas M Babinec, Birgit JM Hausmann, Mughees Khan, Yinan Zhang, Jeronimo R Maze, Philip R Hemmer, and Marko Lončar. A diamond nanowire single-photon source. *Nature nanotechnology*, 5(3):195–199, 2010.

[40] Tim Schröder, Matthew E Trusheim, Michael Walsh, Luozhou Li, Jiabao Zheng, Marco Schukraft, Jose L Pacheco, Ryan M Camacho, Edward S Bielejec, Alp Sipahigil, et al. Scalable focused ion beam creation of nearly lifetime-limited single quantum emitters in diamond nanostructures. *arXiv preprint arXiv:1610.09492*, 2016.

[41] A Sipahigil, RE Evans, DD Sukachev, MJ Burek, J Borregaard, MK Bhaskar, CT Nguyen, JL Pacheco, HA Atikian, C Meuwly, et al. An integrated diamond nanophotonics platform for quantum-optical networks. *Science*, 354(6314):847–850, 2016.

[42] Jin Liu, Macelo Davanco, Luca Sapienza, Kumarasiri Konthasinghe, Jose Vinicius De Miranda Cardoso, Jin Dong Song, Antonio Badolato, and Kartik Srinivasan. Cryogenic photoluminescence imaging system for nanoscale positioning of single quantum emitters. *arXiv preprint arXiv:1612.07412*, 2016.

[43] Sergio Boixo, Sergei V Isakov, Vadim N Smelyanskiy, Ryan Babbush, Nan Ding, Zhang Jiang, John M Martinis, and Hartmut Neven. Characterizing quantum supremacy in near-term devices. *arXiv preprint arXiv:1608.00263*, 2016.